

Direct Imaging and Simulation of the Interface Reaction of Metal/Metal Oxide Nanoparticle Laminates

Haiyang Wang,[†] Prithwish Biswas,[†] and Michael R. Zachariah*

Cite This: *J. Phys. Chem. C* 2022, 126, 8684–8691

Read Online

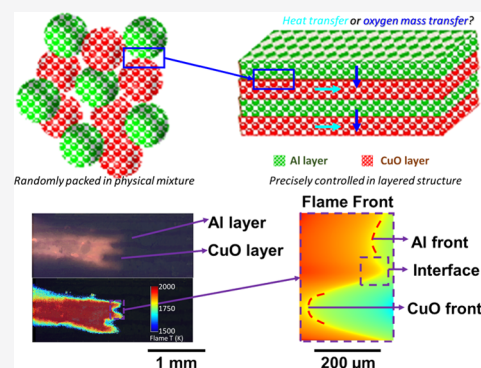
ACCESS |

Metrics & More

Article Recommendations

Supporting Information

ABSTRACT: One of the difficulties in understanding how powder composites of reactive fuel/oxidizer systems behave is the lack of control of the mixing length. In this study, we have prepared Al/CuO particle laminates using a direct writing approach. With as little as 10 wt % polymers, we were able to obtain free-standing microscale particle-based laminates. Using these composites, we were able to image the cross section of the laminates to directly probe the interface reaction with high-speed microscopic imaging and pyrometry. We show quantitatively how the burn rate can be altered by changing the layer thicknesses of the printed laminates and under high-speed microscopy imaging asymmetry heat transfer resulting in fingering in the temperature profiles in the reaction front. Numerical simulations of the heat and mass transport processes are able to reproduce the finger-structured reaction fronts. We find that for Al/CuO particle-based laminates, the lateral O₂ diffusion rate from the CuO layer to the Al layer appears to be rate-limiting. The finger-like profiles appear due to the combined effects from the faster propagation of the interfacial reaction over the bulk, and the thermal diffusivity differences between the Al/CuO layers. Interestingly we see no evidence of layer intermixing even on postcombustion inspection. These results are to our knowledge the first imaging of interface reactions between particle composites and provide a valuable testbed for probing mechanisms and validating models.



INTRODUCTION

One of the difficulties in understanding how powder composites of reactive fuel/oxidizer^{1–6} systems behave is the lack of control of the mixing length. On the other hand, there is a considerable body of work on the formation of nanolaminate structures with alternating reactive layers typically created by sputter deposition. These sputter-deposited reactive nanolaminates consisting of sequential layers of fuel and oxidizers with high energy density have attracted particular attention due to their precisely tunable energy release rate that can be attributed to their highly controllable architecture.^{7–12} In addition to the utility in probing nanothermite reactions, these configurations have also been explored as a method to probe the energy release from binary alloying reactions of Al/Ni,^{13,14} Al/Zr,¹⁵ and Al/Pt.¹⁶ Previous studies have observed that the energy release rate of Al/CuO nanolaminates could be easily adjusted via bilayer thicknesses,¹⁷ equivalence ratios,¹⁸ tertiary interfacial layer insertion,^{19–21} sample width,²² and altering oxidation state of oxidizers.²³

Energetic particulate composites have been extensively investigated through macroscopic characterization approaches to characterize temperature, burn rates, and thermal decomposition properties^{1–22} However, characterization at the microscopic scale has been less readily available. Given that the composition of these composites consists of nano or micro-sized reactants, observation at smaller length scales is needed

to better understand the role of mass and heat transfer.^{2,24–28}

Previously, we employed a recently developed microscopic dynamic imaging system to probe the reaction zone of sputter-deposited Al/CuO nanolaminates with μ s and μ m temporal and spatial resolution respectively, which is more comparable to the reactant dimensions and reaction timescales.²⁹ Through this technique, we obtained detailed images and temperature profiles across the Al/CuO nanolaminates reaction front. However, this system never enabled us to probe and image the cross section which meant we could never directly observe the interface reaction.

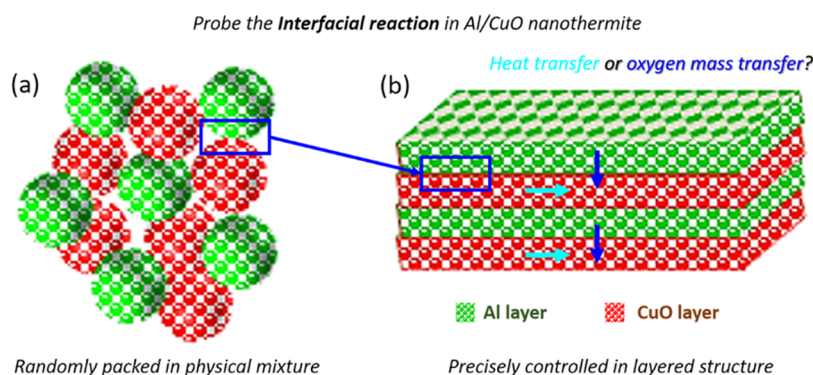
The objective of this paper is twofold. (A) Fabricate microscale particulate laminates with controlled bilayer spacing and sufficient mechanical integrity by direct writing deposition of high loading nanothermite inks. To accomplish this, we explore the utility of three-dimensional (3D) printing for fabrication based on our prior capabilities and the fact that we have been able to prepare similar structures using electrospray deposition.³⁰ (B) Image the cross-sectional interface in

Received: January 8, 2022

Revised: April 20, 2022

Published: May 11, 2022



Scheme 1. Concept of This Study: Imaging the Cross Section of a Particle-Based Laminate Structure During Propagation to Deduce the Controlling Effects of Heat and Oxygen Mass Transfer

operando of the particulate laminates to provide data for benchmark modeling. This then enables us to ask the fundamental questions related to the role of heat and mass transfer on flame propagation of energetic nanocomposites (Scheme 1).

In this study, we prepared Al/CuO particle laminates using a recently developed direct writing approach. Through the first-ever microscopic imaging of the cross section during the reaction, we observed the development of unusual finger-like temperature profiles near the flame front. Macroscopic burn-rate characterizations revealed that the burn rate can be altered by changing the layer thicknesses of the printed laminates, indicating strong effects from oxygen transport between the fuel and oxidizer layer. Using a numerical model of the heat and mass transport during the flame propagation, we have shown that the development of such a finger-shaped profile can be attributed to a combination of (i) faster interfacial reaction than flame propagation in the bulk and (ii) difference in thermal diffusivities between the fuel layer and the oxidizer layer. Both the experiment and model confirmed that O_2 transport is the rate-limiting factor in the reaction propagation of printed laminates. These fundamental insights into the interfacial reaction propagation in energetic laminates, are extremely important to validate mechanisms and models.

2. METHODS

2.1. Materials. Aluminum nanoparticles (Al NPs, 67 wt % active, 81 nm) and CuO nanoparticles (CuO NPs, ~40 nm) are purchased from Novacentrix Inc. And US Research Nanomaterials, respectively. METHOCEL F4M hydroxypropyl methylcellulose (HPMC) and polyvinylidene fluoride (PVDF, $M_w \sim 534,000$) are obtained from Dow Chemical Company and Sigma-Aldrich, respectively. *N,N* dimethylformamide (DMF, 99.8%) is purchased from Sigma-Aldrich and used as a solvent to dissolve the abovementioned polymers.

2.2. Ink Preparation and Direct Writing Approach. Typically, 750 mg of Al or CuO, 50 mg of HPMC, 33 mg of PVDF, and DMF (5 mL and 4 mL of DMF for Al and CuO, respectively) are used for each ink formulation. When preparing the inks, polymer mixtures of HPMC and PVDF in a mass ratio of 3:2 is first added and dissolved in DMF. Then, the weighed CuO NPs or Al NPs are added to form a slurry. A 30 min ultra-sonication step is used to break up nanoparticle aggregates. Then the slurries are magnetically stirred (300 rpm) for 24 h to achieve homogenization prior to printing.

In a typical printing process, the inks are extruded through a 16-gauge needle (ID: 1.35 mm) at a feed rate of 3 mL/h and printed into G-code-patterned square pads (2×2 cm) on a preheated substrate (75°C) at a writing speed of 22 cm/min (moving speed of the nozzle). At this rate, the print is completely dry before depositing another layer. All the laminates have a total thickness of 0.65–0.75 mm but with different bilayer thicknesses of Al/CuO. When printing Al/CuO laminates, Al layers are always printed first on the preheated substrate, followed by the CuO layer, and so on. After printing, the samples are left on the heated substrate (kept at $\sim 75^\circ\text{C}$) for 30 min to further evaporate any remaining solvent. Finally, the pads are peeled off from the substrate and cut into ~ 2 mm wide sticks for combustion characterization. The porosity of all laminates is estimated as $\sim 65\%$ based on our previous studies.^{2,27–29}

2.3. Macroscopic and Microscopic Imaging of the Combustion. The experimental setup used in this study is shown in Figure S1. The samples are free-standing sticks (1.5 cm long, ~ 2 mm wide, and ~ 1 mm thick), which are sandwiched by two thin glass slides (22×22 mm, 1 mm thick) to avoid vibration during the microscopic combustion observation. The sample is confined in a 0.5 L box to enable an inert gas environment of argon. (1 atm) and ignited by a nichrome wire. Two camera systems with macroscopic and microscopic magnifications are triggered simultaneously to obtain videos of a single combustion event. The macroscopic imaging high-speed camera ($80 \mu\text{m}/\text{pixel}$, Vision Research Phantom Miro M110) captures the whole burning event of the stick at a sample rate of 13,000 frames/s (640×200 pixels) to obtain the burn rate and flame temperature, while the microscopic imaging system ($2 \mu\text{m}/\text{pixel}$, Vision Research Phantom VEO710L coupled to an infinity photo-optical model K2 DistaMax) captures the local flame front at a sample rate of 24,000 frames/s (512×512 pixels). The details of using the color filters to obtain temperature maps by pyrometry can be found in our previous studies.^{31,32} Briefly, three-channel intensity (red, green, and blue) ratios (calibrated from a Mikron M390 blackbody source) are extracted to obtain the reaction flame temperature both temporally and spatially from the video images. The threshold errors for data acceptance and false-color temperature assignment are set nominally to ~ 200 – 300 K. The morphologies and compositions of the 3D-printed Al/CuO laminates and their combustion products are characterized by scanning electron microscopy (SEM, Thermo-Fisher Scientific NNS450) coupled with energy-dispersive X-ray spectroscopy (EDS).

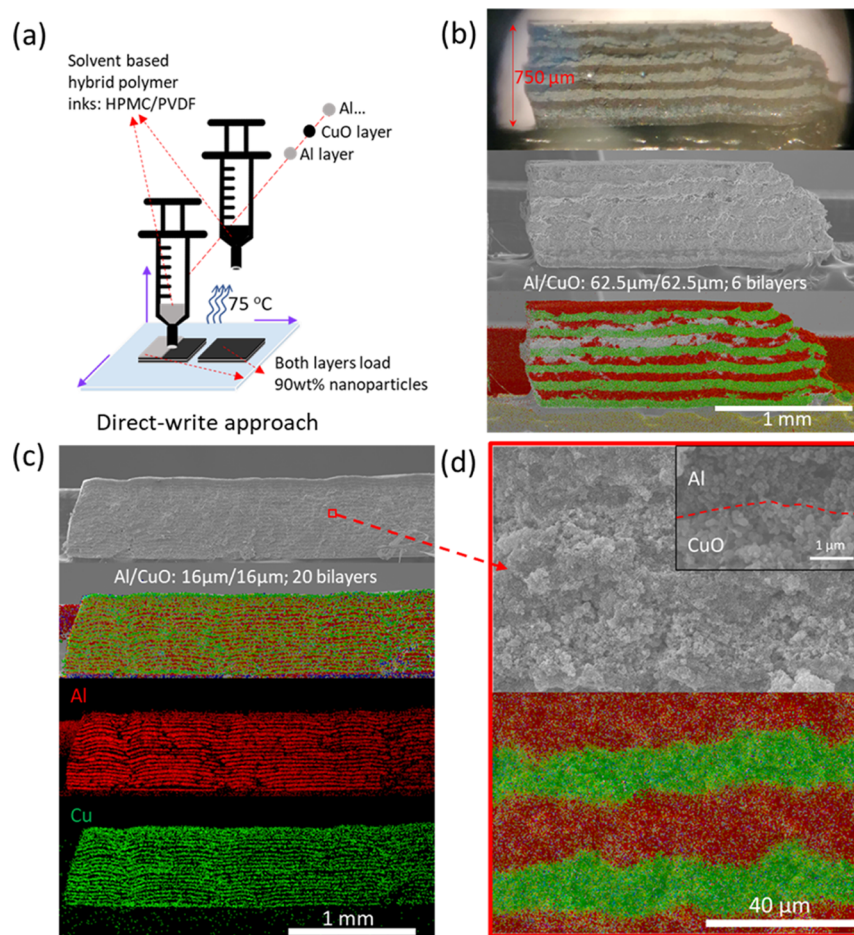


Figure 1. Direct-write approach of Al/CuO high loading particle laminates (a); optical, SEM, and EDS images of Al/CuO particle laminates with a bilayer thickness of 125 μm (b); low (c) and higher (d) magnification SEM and EDS images with a bilayer thickness of 32 μm . Note: the image of Al/CuO laminate with a bilayer thickness of 187.5 μm is shown in Figure S3. The total laminate thickness for 20 bilayers of Al/CuO (bilayer thickness: 32 μm) is ~ 650 μm .

2.4. Simulation of Reaction Propagation in Particle Laminates. In order to model the energy and mass transfer processes leading to reaction propagation in the particle laminates, we have considered a two-dimensional (2D) single bilayer of Al/CuO particles as a solution domain (Figure S2). Periodic boundary conditions have been considered in the z -direction such that the energy and mass fluxes exiting across the top boundary of the Al layer enters through the bottom boundary of the CuO layer and conversely those exiting through the bottom of the CuO layer enter the Al layer from the top. These conditions ensure the elimination of edge effects, thereby representing the case of a laminate containing multiple bilayers. Energy transfer and the temperature profile (T) of the laminates have been modeled by the 2D temporal reaction-diffusion energy equation eq 1

$$\alpha_i \left(\frac{\partial^2 T}{\partial x^2} + \frac{\partial^2 T}{\partial z^2} \right) + \left(\frac{-r_i''' \Delta H_i}{\rho_i C_p} \right) = \frac{\partial T}{\partial t}; \quad [i = \text{Al}, \text{CuO}] \quad (1)$$

where the source term is either heat generation due to Al-oxidation ($\Delta H = -838$ kJ/mol) in the Al layer or heat dissipation due to endothermic CuO decomposition in the CuO-layer ($\Delta H = 156$ kJ/mol). R_i''' is the volumetric consumption rate ($\text{mol}/\text{m}^3\text{s}$) of either Al or CuO due to

oxidation or decomposition, respectively, and the negative sign treats the inverse relation between the sign of enthalpy (ΔH_i) and heat generation. For simplicity, density (ρ_i) and mass-specific heat (C_p) of bulk Al (~ 2700 kg/ m^3 and 890 J/kg K) and CuO (~ 6310 kg/ m^3 and 695 J/kg K) have been used for the corresponding layers, while thermal diffusivity (α_i) has been used as a free-parameter and optimized based on experimental data. Although the thermal diffusivities have been varied as a free parameter, the ratio of thermal diffusivities between the Al and CuO layer has been kept constant at 10:1, corresponding to bulk Al and CuO. As the Al-oxidation rate is dependent on the availability of oxygen in the Al layer, the mass-transfer and concentration profile (C_{O_2}) of oxygen has been modeled by eq 2

$$D_i \left(\frac{\partial^2 C_{\text{O}_2}}{\partial x^2} + \frac{\partial^2 C_{\text{O}_2}}{\partial z^2} \right) + r_{\text{O}_2}''' = \frac{\partial C_{\text{O}_2}}{\partial t}; \quad [i = \text{Al}, \text{CuO}] \quad (2)$$

where D_i is O_2 diffusivity in either the Al or CuO layer and r_{O_2}''' is the volumetric O_2 generation/dissipation rate in either CuO or Al layer. We have assumed that the initial free concentration of O_2 is null and the O_2 generated from the decomposition of CuO only diffuses through the pores in the CuO layer having a porosity (ϵ) of 0.65. Therefore, we estimated an effective O_2

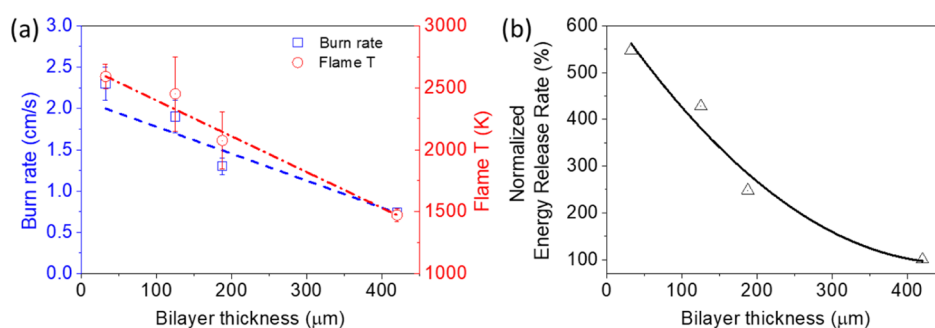


Figure 2. Burn rate, flame T (a), and energy release rate (b) change with bilayer thickness

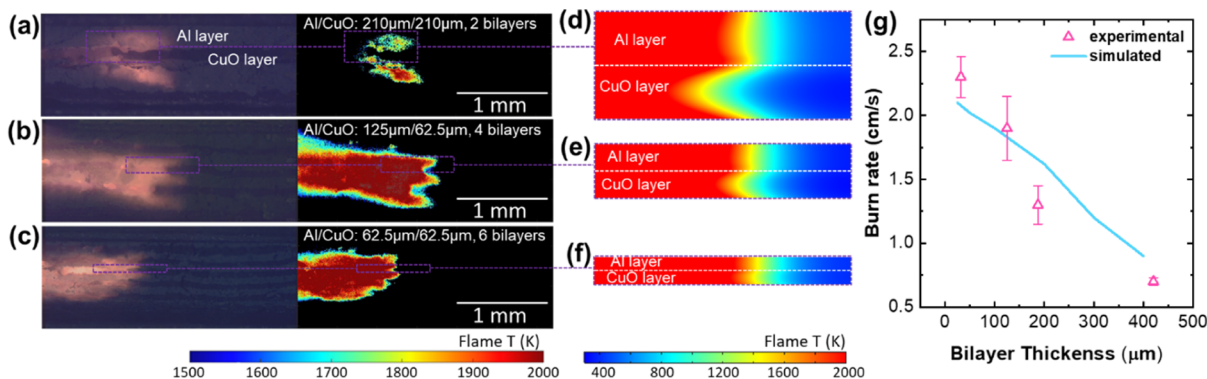


Figure 3. Typical microscopic snapshots and their corresponding temperature maps (a–c) indicate the “finger” structures of the flame front 2 (a), 4 (b), and 6 (c) bilayers (bilayer thickness is 420, 187.5, and 125 μm , respectively). Numerical computations (d–f) reveal a similar “finger” structure of the flame propagation with a similar bilayer thickness of 400 (d), 200 I, and 100 μm (f). Experimental and simulated burn rates change with increasing bilayer thickness (g).

diffusivity in the CuO layer, $D_{\text{eff}} = \frac{\epsilon}{\epsilon^{-1/3}} D_{\text{O}_2}$, through the Millington-Quirk tortuosity model,³³ where $D_{\text{O}_2} \sim 2 \times 10^{-5} \text{ m}^2/\text{s}$ is the molecular diffusivity of O_2 at standard temperature and pressure (NIST) and a $D_{\text{O}_2} = D_{\text{O}_2}(T/298)^{1.5}$ temperature dependence. The diffusivity value of O_2 ($\sim 10^{-18} \text{ m}^2/\text{s}$) in solid Al_2O_3 ³⁴ has been used for solving eq 2 in the Al layer.

Whenever C_{O_2} is non-zero in the Al layer, Al is assumed to oxidize at a critical reaction rate, $r_{\text{Al}}''' \sim 6 \times 10^6 \text{ mol}/\text{m}^3\text{s}$, obtained from the critical rate determined from a previous study³⁵ assuming a particle size of 50 nm. The CuO decomposition has been assumed to follow a zero-order rate law, $r_{\text{CuO}}''' = k_0 \exp(-E_a/RT) \text{ mol}/\text{m}^3\text{s}$, with the Arrhenius pre-exponential factor (k_0) the same as r_{Al}''' with an activation energy (E_a) of $\sim 125 \text{ kJ}/\text{mol}$.³⁶ Hence, the rate of O_2 generation in the CuO layer is $r_{\text{O}_2\text{CuO}}''' = 0.5 r_{\text{CuO}}'''$, whereas the rate of O_2 dissipation in the Al layer is $r_{\text{O}_2\text{Al}}''' = -0.75 r_{\text{Al}}'''$, by accounting for the stoichiometries of the respective reactions. For simplicity, both the CuO decomposition (high heating rate O_2 release $\sim 940 \text{ K}$)³⁶ and Al-oxidation are assumed to initiate at $T = 923 \text{ K}$, which is the melting point of Al. The left boundary condition for the energy equation (eq 1) has been assumed to be a constant temperature of $T = 2100 \text{ K}$, which is the experimentally observed average flame temperature. A constant convective heat flux to the ambient at $T = 298 \text{ K}$ with $h = 1 \text{ W}/\text{K}$, has been imposed as the right boundary condition of eq 1. No-flux conditions has been imposed on both left and right boundaries for solution of eq 2. $T = 298 \text{ K}$ and $\text{C}_{\text{O}_2} = 0$ has been used as initial conditions for solving eqs 1 and 2, respectively. The coupled eqs 1 and 2 with the above-

mentioned parameters and boundary conditions were solved using COMSOL.

3. RESULTS AND DISCUSSION

3.1. Microscale Al/CuO Particle Laminates. Figure 1a shows the direct writing approach, which is formulated based on our previous studies.^{2,27–29} The only difference is that we used two syringes/nozzles to alternatively deposit Al or CuO on the preheated substrate. Inks in both the syringes contain 10 wt % polymer mixtures of HPMC and PVDF and 90 wt % nanoparticles of Al or CuO. The typical optical, SEM, and EDS images of the resulting Al/CuO laminates with a different bilayer thickness of 125 and 32 μm are shown in Figure 1b,c, respectively. A more zoomed-in view of the thinnest bilayer (32 μm) of Al/CuO particle laminate is shown in Figure 1d. These images demonstrate that well-layered Al and CuO particle laminates can be prepared, and the interface between Al and CuO layers is clear and does not show overlap between the layers.

The burn rate and flame temperature of the Al/CuO laminates are obtained from macroscopic burning of the composite sticks with different bilayer thicknesses (Figure 2a, more details in Supporting Information Video S1). With the increase of bilayer thickness, both the burn rate and flame temperature decrease monotonically. The burn rate reduces by a factor of 3 when the bilayer thickness changes from 32 μm (2.3 cm/s) to 420 μm (0.7 cm/s). Over this range the flame temperature drops from 2500 to 1500 K. Considering that the density is roughly the same for all the laminates, the normalized energy release rate (Figure 2b) also decreases with increasing bilayer thickness. Details about the burn

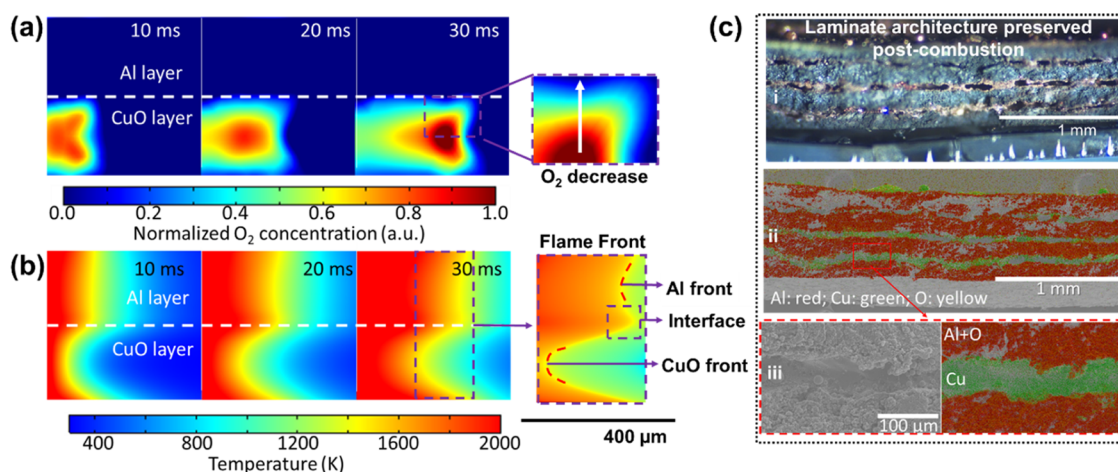


Figure 4. (a) Computed time-resolved O₂ concentration showing a decrease in its concentration from the center of the CuO layer to the interface; (b) computed temperature map showing the different features of the flame front at the Al-layer, CuO-layer, and the interface. (c) Optical image after combustion (i) and its EDS mapping result (ii,iii) show that the laminate architecture (187 μm bilayer) is preserved postcombustion and the products AlO_x and Cu remain in separate layers.

behavior of premixed films can be found in our previous work.³⁷

3.2. Temperature Distribution from Experiments and Simulation. A typical microscopic image and its temperature map of the cross section (bilayer thickness of 420, 187.5, and 125 μm) is shown in Figures 3a–3c (Supporting Information Video S2). The snapshots clearly show a “finger”-like structure in the flame front, with the Al layer proceeding ahead of the CuO layer. The reason for the lagging effects of the CuO layer on the flame front is that the heat generated from the interface reaction conducts differently in the Al and CuO layers. Because the CuO layer undergoes a latent decomposition process, the temperature will lag as it first decomposes before energy can go to sensible heating.

The numerical model (Section 2.4) as outlined above was solved over 100 ms, to obtain a spatiotemporal temperature profile. Figure 3d–f shows the spatial temperature distribution with different bilayer thicknesses after 40 ms of propagation. The computed (Figure 3) reaction front in the CuO-layer lags the reaction front in the Al layer giving rise to a finger-like profile, consistent with the experimental flame front. Figure 3g shows both experimental and calculated burn rates from Al/CuO laminates with different bilayer thicknesses and shows that experimental data matches well with the calculation. The computed burn rate decreases linearly with increasing bilayer thicknesses, showing the same trend as observed in experiments. In the numerical solution, the absolute values of thermal diffusivities of the Al and CuO layers (preserving the 10:1 ratio) have been optimized ($\alpha_{Al} \sim 5.1 \times 10^{-6} \text{ m}^2/\text{s}$) to match the computed burn rate with experimental burn rates. The sensitivity of the computed burn rate to the thermal diffusivity has been analyzed later. With increasing bilayer thickness, the O₂ diffusion rate from the CuO layer to the Al layer decreases correspondingly, thereby possibly reducing the rate of mixing between the fuel and oxidizer. The role of this diffusion limitation as a major controlling factor on the overall reaction rate is further evaluated in the subsequent sections.

The characteristic “finger” is also observed in both the microscopic experiment and computational results. Generally, the thicker bilayers show a slow burning rate and enhanced finger-like profile. When the bilayer thickness is as small as 30 μm, we barely see any finger structures on the flame front

(Figure S4). The finger-like profile may appear as a result of (i) difference in reaction propagation rates at the interface and the bulk (ii) thermal diffusivity difference (10×) between the layer, the mechanism of which is analyzed in the next section.

3.3. O₂ Diffusion and Interface Reaction. We now turn to a mechanistic interpretation to further explain our observations. The computationally determined time-resolved O₂ concentration and temperature profiles obtained from the numerical solution are shown in Figure 4a,b, respectively. Figure 4a shows the concentration profile of O₂ in the 400 μm bilayers case, at different times. During the reaction, a maximum O₂ concentration is observed at the center of the CuO layer (Figure 4a and Supporting Information Video S3) and is depleted toward the interfacial boundary. This implies that O₂ consumption by Al is faster than can be replenished by the center of the CuO layer. This effect can also be observed in the computed temperature distribution (Figure 4b and Supporting Information Video S4). Three distinct features are observed on the temperature profile of the flame front: (i) short projections (~10 μm) near the Al/CuO interfacial boundary, which propagate ahead of the rest of the reaction front (ii) reaction front in the Al layer which lags a little (~10 μm) behind the interfacial front giving rise to the finger-like profile observed experimentally (iii) the CuO front which lags far behind the Al front (~100 μm).

By simulating an ideal but unrealistic case where the thermal diffusivity is the same everywhere, but keeping the other mass transfer parameters the same, we find that small projections from the propagation front still appear at the interfacial boundary (Figure S5). This implies that the smaller projections appear due to the faster reaction propagation at the interfacial boundary. Hence, during the combustion of particulate laminates, the reaction is initiated at the interfacial boundary of the fuel-oxidizer layers. The higher (~10×) thermal diffusivity of the Al layer propagates the heat generated at the interface faster across the bulk of the layer causing the Al front to propagate ahead of the CuO front creating a finger-like profile. In fully dense nanolaminates, these fingering flame fronts have not been experimentally observed, because the propagation is not diffusion-limited due to the short distances (nanoscale) between fuel and oxidizer. Rather, it is the decomposition rate of CuO that is rate controlling.³⁸ In our

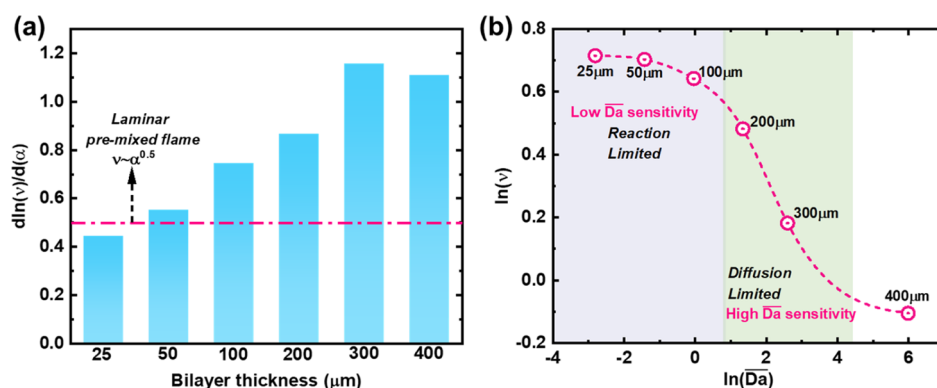


Figure 5. (a) Sensitivity of burn rate to thermal diffusivity increases with the increase in bilayer thickness (b) sensitivity of the burn rate to the Damköhler number shows a clear transition from reaction limitation to diffusion limitation with the increase in bilayer thickness.

case, the particulate laminates have a relatively long diffusion distance between Al and CuO layers, making the decomposition characteristic time negligible compared to the time of diffusion.

An optical image of the post-combustion laminate [Figure 4c(i)] along with its EDS mapping results [Figure 4c(ii,iii)] indicate that upon burning, the Al and CuO layer become Al_2O_3 and Cu layers respectively, retaining their respective positions in the laminate architecture without mixing. This implies that during the combustion, CuO decomposes and the released O_2 diffuses to the Al layer initiating the oxidation process. In the model, the absence of O_2 in the Al layer (Figure 4a), suggests that the oxidation occurs more rapidly than the mass transfer of O_2 to the Al layer. Therefore, we may conclude that the combustion rate of Al/CuO particle laminates is limited by the O_2 diffusion rate. Hence, with increasing bilayer thickness, the increased O_2 diffusion distance reduces the overall burn rate, as observed in Section 2.2. An EDS image of the interface (Figure S6) shows that the condensed phase mixing between Al and CuO is only limited to a short distance $<10 \mu\text{m}$ from the interface for a bilayer thickness of $\sim 188 \mu\text{m}$ (5% of bilayer thickness) and, thereby, has negligible impact on the overall reaction propagation. This justifies having neglected interfacial mixing in our simulation.

3.4. Sensitivity of the Burn Rate to Heat Transfer and O_2 Diffusion. The numerical solution of the burn rate is dependent on various parameters such as thermal diffusivity of the Al layer (α_{Al}), thermal diffusivity of the CuO layer (α_{CuO}), O_2 diffusivity in the CuO layer, O_2 diffusivity in the Al layer, the decomposition rate of CuO, and the oxidation rate of Al. Values obtained from in situ measurements as reported in previous studies^{35,36} have been used for these parameters, whereas the thermal diffusivities have been adjusted to match the numerical results with experiments (Section 3.2). Figure S7a shows the burn rates obtained for various bilayer thicknesses when the thermal diffusivity of the Al layer is perturbed to $0.68\times$ and $0.1\times$ times its optimized value (best fit to experimental results). A significant difference is observed in the burn rates of all the bilayer thicknesses on changing this parameter. However, Figure S7b shows that the O_2 diffusion coefficient in the CuO layer does not have a significant effect on the absolute burn rate value, indicating that the mass transfer rate of O_2 from the CuO layer to the Al layer is mostly dependent on the length of the diffusion barrier.

To quantitatively identify the sensitivity of the burn rates at different bilayer thicknesses, we have computed a sensitivity

coefficient for the thermal diffusivity, $S_\alpha = d\ln v/d\ln \alpha$, where v and α are the burn-velocity and thermal diffusivity, respectively. The evaluated sensitivity coefficient obtained from linear fitting ($R^2 > 0.99$) of the values in Figure S7a is shown in Figure 5a. According to laminar premixed flame theory, $v \sim \sqrt{\alpha}$ and, hence, the sensitivity coefficient, $S_\alpha = d\ln v/d\ln \alpha \sim 0.5$. However, Figure 5a shows that the burn rate of the laminates scales with thermal diffusivity as $v \sim \alpha^x$, where x increases (~ 0.4 to 1.1) with the increase in bilayer thickness. This indicates that the sensitivity of the burn rate to thermal diffusivity increases with increasing bilayer thickness.

Because the propagation is limited by O_2 diffusion, the rate of O_2 transport to the Al layer and the rate of O_2 uptake in the Al layer (or oxidation rate) will have major influence on the burn rate. Here, we express this in the form of an average

Damköhler number, $\overline{\text{Da}} = \frac{r''_{\text{O}_2, \text{Al}} t_z^2}{D_{\text{O}_2, \text{CuO}} C_0}$, based on the ratio of these

two rates, for various bilayer thicknesses (details in Supporting Information). Here, $r''_{\text{O}_2, \text{Al}}$, t_z , $D_{\text{O}_2, \text{CuO}}$, and C_0 , implies the Al oxidation rate, bilayer-thicknesses, O_2 diffusivity in the CuO layer, and maximum O_2 concentration in the center of the CuO layer respectively. As there is a nonlinear dependence of burn rate on $\overline{\text{Da}}$, to perform a sensitivity analysis, we present the results in terms of the natural logarithms in Figure 5b. The derivative of this sigmoidal curve is of course the sensitivity of the burn rate to the Damköhler number. The slope of the curve increases with bilayer thickness, indicating an increasing sensitivity of burn rate to the Damköhler number in the high Damköhler number or mass-transfer limited regime. For bilayer thicknesses of $25\text{--}100 \mu\text{m}$, the $\overline{\text{Da}} \ll 1$, indicating reaction limitation, whereas bilayer thicknesses $>100 \mu\text{m}$ with $\overline{\text{Da}} \gg 1$, are limited by diffusion of O_2 to the Al layer. Hence, with increase in bilayer thickness, mass transfer control increases, and the flame propagation behavior deviates from that of laminar premixed flames. The sensitivity of the burn rate to the $\overline{\text{Da}}$ shows a dip at the $400 \mu\text{m}$ bilayer, which maybe a mathematical artefact due to the low burn rate there. Because the absolute value of the burn rate is small, the relative change in the burn rate value on changing of $\overline{\text{Da}}$ is also small. Hence, the efficient working range of this sensitivity analysis is limited to bilayer thicknesses of less than $300 \mu\text{m}$.

As mentioned previously, Al/CuO sputter-deposited nanolaminates have attracted a considerable number of studies owing to their precisely adjustable reactivity through the bilayer thickness.^{2,24–28} We now compare our particle

laminates with those of prior studies. Figure 6 summarizes the burn rate and energy release rate (normalized based on the

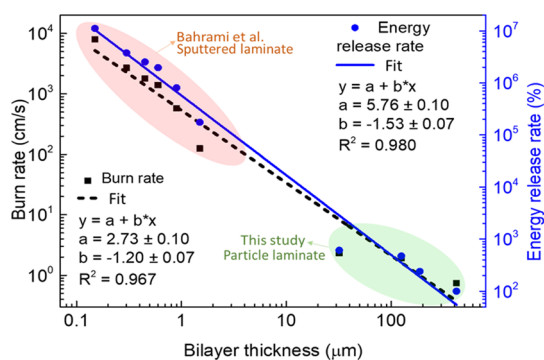


Figure 6. Burn rate and normalized energy release rate as a function of bilayer thickness from nano to micro. The data points of Al/CuO sputter-deposited nanolaminates are from Bahrami et al.,¹⁸ while this study examines particle-based laminates.

burn rate \times density \times flame temperature) with different bilayer thicknesses ranging from 0.15 to 420 μm . Figure 6 shows that both the burn rate and energy release rate can be fit over 3 orders of magnitude in bilayer thickness, leading to a 5-order of magnitude change in both the burn rate and energy release rate. The slope for energy release rate is higher than that of burn rate, mainly owing to the higher density of Al/CuO nanolaminates (4 \times) compared to porous particulate laminates in this study. The results further confirm that the mass transfer from oxidizer to fuel layer is dominating the reaction and flame propagation of the reactive laminates. The differences between the nanolaminates and particulate laminates are the mass transfer mechanism, while the former is controlled by diffusion of condensed phase oxygen ions,¹⁷ the latter is controlled by gas-phase O_2 diffusion.

4. CONCLUSIONS

In this study, we prepared free-standing microscale Al/CuO particle laminates with precise control of interfacial contact between fuel and oxidizer using a simple direct writing approach. With small (10 wt %) polymer additions in each layer of the laminates, we obtain free-standing microscale laminates with burn rates on the order of $\sim\text{cm/s}$, making it easier to observe the cross section of the flame front at the Al/CuO interface. We find that the burn rate can be altered by changing the layer thicknesses of the printed laminates, indicating effects from oxygen transport between the fuel and oxidizer layer, the evidence of which is also observed in postcombustion materials. Through microscopic imaging of the flame propagation in 3D printed Al/CuO laminates as a typical model system, we observed the development of unusual finger-like temperature profiles near the flame front. Through a numerical model of the heat and mass transport processes during the flame propagation in laminates, we have successfully reconstructed these finger-structured flame fronts. We conclude that such a finger-shaped profile can be attributed to a combination of (i) faster propagation of the interfacial reaction than the bulk and (ii) difference in thermal diffusivities of the fuel-oxidizer layers, which has been also confirmed by the ex-situ analysis of combustion products. Both the experiment and model confirmed that O_2 transport is the

rate-limiting factor in the reaction propagation of printed laminates.

■ ASSOCIATED CONTENT

Supporting Information

The Supporting Information is available free of charge at <https://pubs.acs.org/doi/10.1021/acs.jpcc.2c00156>.

Microscopic and macroscopic imaging system; geometry of the solution domain with boundary conditions; microscopic imaging snapshots of Al/CuO laminates with a bilayer thicknesses of 32 μm ; zoomed-in smaller finger structure in the interface of Al/CuO layers; and relationship between computed burn rate and bilayer thicknesses for different thermal diffusivities and O_2 diffusivities (PDF)

Macroscopic imaging of Al/CuO laminates with different bilayer thicknesses (MP4)

Microscopic imaging of Al/CuO laminates with different bilayer thicknesses (MP4)

Computed temporal concentration profile of O_2 in the 400 μm bilayers case (MP4)

Temperature distribution in the 400 μm bilayers case (MP4)

■ AUTHOR INFORMATION

Corresponding Author

Michael R. Zachariah – Department of Chemical and Environmental Engineering, University of California, Riverside, California 92521, United States; orcid.org/0000-0002-4115-3324; Email: mrz@engr.ucr.edu

Authors

Haiyang Wang – Department of Chemical and Environmental Engineering, University of California, Riverside, California 92521, United States; orcid.org/0000-0001-5200-3965

Prithwish Biswas – Department of Chemical and Environmental Engineering, University of California, Riverside, California 92521, United States; orcid.org/0000-0002-9921-2905

Complete contact information is available at: <https://pubs.acs.org/doi/10.1021/acs.jpcc.2c00156>

Author Contributions

[†]H.W. and P.B. are contributed equally.

Notes

The authors declare no competing financial interest.

■ ACKNOWLEDGMENTS

We gratefully acknowledge support from AFOSR. We also thank the CFAMM at the University of California, Riverside, for their microscopy support.

■ REFERENCES

- (1) Wang, H.; Jian, G.; Egan, G. C.; Zachariah, M. R. Assembly and Reactive Properties of Al/CuO Based Nanothermite Microparticles. *Combust. Flame* **2014**, *161*, 2203–2208.
- (2) Wang, H.; Kline, D. J.; Biswas, P.; Zachariah, M. R. Connecting Agglomeration and Burn Rate in a Thermite Reaction: Role of Oxidizer Morphology. *Combust. Flame* **2021**, *231*, 111492.
- (3) Ghildiyal, P.; Ke, X.; Biswas, P.; Nava, G.; Schwan, J.; Xu, F.; Kline, D. J.; Wang, H.; Mangolini, L.; et al. Silicon Nanoparticles for the Reactivity and Energetic Density Enhancement of Energetic-

Biocidal Mesoparticle Composites. *ACS Appl. Mater. Interfaces* **2021**, *13*, 458–467.

(4) Xu, F.; Nava, G.; Biswas, P.; Dulalia, I.; Wang, H.; Alibay, Z.; Gale, M.; Kline, D. J.; Wagner, B.; Mangolini, L.; Zachariah, M. R. Energetic Characteristics of Hydrogenated Amorphous Silicon Nanoparticles. *Chem. Eng. J.* **2022**, *430*, 133140.

(5) Xu, F.; Hirt, B.; Biswas, P.; Kline, D. J.; Yang, Y.; Wang, H.; Sehrioglu, A.; Zachariah, M. R. Superior Reactivity of Ferroelectric Bi₂WO₆/Aluminum Metastable Intermolecular Composite. *Chem. Eng. Sci.* **2022**, *247*, 116898.

(6) Biswas, P.; Ghildiyal, P.; Kwon, H.; Wang, H.; Alibay, Z.; Xu, F.; Wang, Y.; Wong, B. M.; Zachariah, M. R. Rerouting Pathways of Solid-State Ammonia Borane Energy Release. *J. Phys. Chem. C* **2021**, *126*, 48–57.

(7) Rossi, C. Engineering of Al/CuO Reactive Multilayer Thin Films for Tunable Initiation and Actuation. *Propellants, Explos., Pyrotech.* **2019**, *44*, 94–108.

(8) Zapata, J.; Nicollet, A.; Julien, B.; Lahiner, G.; Esteve, A.; Rossi, C. Self-Propagating Combustion of Sputter-Deposited Al/CuO Nanolaminates. *Combust. Flame* **2019**, *205*, 389–396.

(9) Egan, G. C.; Mily, E. J.; Maria, J.-P.; Zachariah, M. R. Probing the Reaction Dynamics of Thermite Nanolaminates. *J. Phys. Chem. C* **2015**, *119*, 20401–20408.

(10) Tai, Y.; Xu, J.; Wang, F.; Dai, J.; Zhang, W.; Ye, Y.; Shen, R. Experimental and Modeling Investigation on the Self-Propagating Combustion Behavior of Al-MoO₃ Reactive Multilayer Films. *J. Appl. Phys.* **2018**, *123*, 235302.

(11) Xu, J.; Shen, Y.; Wang, C.; Dai, J.; Tai, Y.; Ye, Y.; Shen, R.; Wang, H.; Zachariah, M. R. Controlling the Energetic Characteristics of Micro Energy Storage Device by in Situ Deposition Al/MoO₃ Nanolaminates with Varying Internal Structure. *Chem. Eng. J.* **2019**, *373*, 345–354.

(12) Adams, D. P. Reactive Multilayers Fabricated by Vapor Deposition: A Critical Review. *Thin Solid Films* **2015**, *576*, 98–128.

(13) Grapes, M. D.; Weihs, T. P. Exploring the Reaction Mechanism in Self-Propagating Al/Ni Multilayers by Adding Inert Material. *Combust. Flame* **2016**, *172*, 105–115.

(14) Kim, J. S.; Lagrange, T.; Reed, B. W.; Knepper, R.; Weihs, T. P.; Browning, N. D.; Campbell, G. H. Direct Characterization of Phase Transformations and Morphologies in Moving Reaction Zones in Al/Ni Nanolaminates Using Dynamic Transmission Electron Microscopy. *Acta Mater.* **2011**, *59*, 3571–3580.

(15) Overdeep, K. R.; Schmauss, T. A.; Panigrahi, A.; Weihs, T. P. The Influence of Sample Thickness on the Combustion of Al:Zr and Al-8Mg:Zr Nanolaminate Foils. *Combust. Flame* **2018**, *196*, 88–98.

(16) Abernethy, M. J.; Yarrington, C. D.; Adams, D. P. Heating Rate Dependent Ignition of Al/Pt Nanolaminates through Pulsed Laser Irradiation. *J. Appl. Phys.* **2018**, *123*, 235304.

(17) Lahiner, G.; Nicollet, A.; Zapata, J.; Marín, L.; Richard, N.; Rouhani, M. D.; Rossi, C.; Estève, A. A Diffusion–Reaction Scheme for Modeling Ignition and Self-Propagating Reactions in Al/CuO Multilayered Thin Films. *J. Appl. Phys.* **2017**, *122*, 155105.

(18) Bahrami, M.; Taton, G.; Conédéra, V.; Salvagnac, L.; Tenailleau, C.; Alphonse, P.; Rossi, C. Magnetron Sputtered Al-CuO Nanolaminates: Effect of Stoichiometry and Layers Thickness on Energy Release and Burning Rate. *Propellants, Explos., Pyrotech.* **2014**, *39*, 365–373.

(19) Marín, L.; Nanayakkara, C. E.; Veyan, J.-F.; Warot-Fonrose, B.; Joulie, S.; Estève, A.; Tenailleau, C.; Chabal, Y. J.; Rossi, C. Enhancing the Reactivity of Al/CuO Nanolaminates by Cu Incorporation at the Interfaces. *ACS Appl. Mater. Interfaces* **2015**, *7*, 11713–11718.

(20) Marín, L.; Warot-Fonrose, B.; Estève, A.; Chabal, Y. J.; Rodriguez, L. A.; Rossi, C. Self-Organized Al₂Cu Nanocrystals at the Interface of Aluminum-Based Reactive Nanolaminates to Lower Reaction Onset Temperature. *ACS Appl. Mater. Interfaces* **2016**, *8*, 13104–13113.

(21) Lanthony, C.; Guiltat, M.; Ducéré, J. M.; Verdier, A.; Hémerlyck, A.; Djafari-Rouhani, M.; Rossi, C.; Chabal, Y. J.; Estève, A. Elementary Surface Chemistry during CuO/Al Nanolaminate-

Thermite Synthesis: Copper and Oxygen Deposition on Aluminum (111) Surfaces. *ACS Appl. Mater. Interfaces* **2014**, *6*, 15086–15097.

(22) Xu, J.; Tai, Y.; Ru, C.; Dai, J.; Shen, Y.; Ye, Y.; Shen, R.; Fu, S. Characteristic of Energetic Semiconductor Bridge Based on Al/MoO₃ Energetic Multilayer Nanofilms with Different Modulation Periods. *J. Appl. Phys.* **2017**, *121*, 113301.

(23) Blobaum, K. J.; Reiss, M. E.; Plitzko, J. M.; Weihs, T. P. Deposition and Characterization of a Self-Propagating CuOx/Al Thermite Reaction in a Multilayer Foil Geometry. *J. Appl. Phys.* **2003**, *94*, 2915.

(24) Grapes, M. D.; Lagrange, T.; Friedman, L. H.; Reed, B. W.; Campbell, G. H.; Weihs, T. P.; Lavan, D. A. Combining Nanocalorimetry and Dynamic Transmission Electron Microscopy for in Situ Characterization of Materials Processes under Rapid Heating and Cooling. *Rev. Sci. Instrum.* **2014**, *85*, 084902.

(25) Santala, M. K.; Grapes, M. D.; Weihs, T. P.; Reed, B. W.; Lagrange, T.; Campbell, G. H. Imaging Unsteady Propagation of Reaction Fronts in Reactive Multilayer Foils with Multi-Frame Dynamic TEM. *Microsc. Microanal.* **2014**, *20*, 1584–1585.

(26) Pauls, J. M.; Shuck, C. E.; Genç, A.; Rouvimov, S.; Mukasyan, A. S. In-Situ Transmission Electron Microscopy Determination of Solid-State Diffusion in the Aluminum-Nickel System. *J. Solid State Chem.* **2019**, *276*, 114–121.

(27) Wang, H.; Kline, D. J.; Zachariah, M. R. In-Operando High-Speed Microscopy and Thermometry of Reaction Propagation and Sintering in a Nanocomposite. *Nat. Commun.* **2019**, *10*, 3032.

(28) Wang, H.; Kline, D. J.; Rehwoldt, M. C.; Zachariah, M. R. Carbon Fibers Enhance the Propagation of High Loading Nanothermites: In Situ Observation of Microscopic Combustion. *ACS Appl. Mater. Interfaces* **2021**, *13*, 30504–30511.

(29) Wang, H.; Julien, B.; Kline, D. J.; Alibay, Z.; Rehwoldt, M. C.; Rossi, C.; Zachariah, M. R. Probing the Reaction Zone of Nanolaminates at $\sim\mu\text{s}$ Time and $\sim\mu\text{m}$ Spatial Resolution. *J. Phys. Chem. C* **2020**, *124*, 13679–13687.

(30) Li, X.; Guerrieri, P.; Zhou, W.; Huang, C.; Zachariah, M. R. Direct Deposit Laminate Nanocomposites with Enhanced Propellant Properties. *ACS Appl. Mater. Interfaces* **2015**, *7*, 9103–9109.

(31) Jacob, R. J.; Kline, D. J.; Zachariah, M. R. High Speed 2-Dimensional Temperature Measurements of Nanothermite Composites: Probing Thermal vs. Gas Generation Effects. *J. Appl. Phys.* **2018**, *123*, 115902.

(32) Kline, D. J.; Rehwoldt, M. C.; Wang, H.; Eckman, N. E.; Zachariah, M. R. Why Does Adding a Poor Thermal Conductor Increase Propagation Rate in Solid Propellants? *Appl. Phys. Lett.* **2019**, *115*, 114101.

(33) Millington, R. J.; Quirk, J. P. Permeability of Porous Solids. *Trans. Faraday Soc.* **1961**, *57*, 1200–1207.

(34) Lee, K.; Stewart, D. S. Modeling Aluminum Combustion in Oxidizing Environment with the Gibbs Formulation. *Combust. Flame* **2020**, *220*, 92–106.

(35) Jian, G.; Zhou, L.; Piekil, N. W.; Zachariah, M. R. Low Effective Activation Energies for Oxygen Release from Metal Oxides: Evidence for Mass-Transfer Limits at High Heating Rates. *ChemPhysChem* **2014**, *15*, 1666–1672.

(36) Zhou, W.; DeLisio, J. B.; Wang, X.; Egan, G. C.; Zachariah, M. R. Evaluating Free vs Bound Oxygen on Ignition of Nano-Aluminum Based Energetics Leads to a Critical Reaction Rate Criterion. *J. Appl. Phys.* **2015**, *118*, 114303.

(37) Wang, H.; Shen, J.; Kline, D. J.; Eckman, N.; Agrawal, N. R.; Wu, T.; Wang, P.; Zachariah, M. R.; Wang, H.; Zachariah, M. R.; Shen, J.; Kline, D. J.; Eckman, N.; Agrawal, N. R.; Wu, T.; Wang, P. Direct Writing of a 90 Wt% Particle Loading Nanothermite. *Adv. Mater.* **2019**, *31*, 1806575.

(38) Tichtchenko, E.; Estève, A.; Rossi, C. Modeling the Self-Propagation Reaction in Heterogeneous and Dense Media: Application to Al/CuO Thermite. *Combust. Flame* **2021**, *228*, 173–183.